Binding Mechanisms of Trivalent Chromium on Colloidal Phases from Ultramafic Systems: Insights from Batch Experiments and XAS Analysis

Thi Tuyen Nguyen, Rémi Marsac, Alexis Groleau, Jaimy Scaria, Yann Sivry

Journal Pre-proof

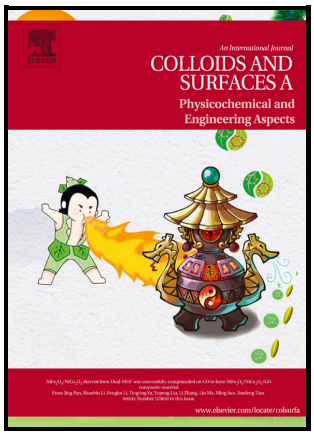

Binding Mechanisms of Trivalent Chromium on Colloidal Phases from Ultramafic Systems: Insights from Batch Experiments and XAS Analysis

Thi Tuyen Nguyen, Rémi Marsac, Alexis Groleau, Jaimy Scaria, Yann Sivry

PII: S0927-7757(24)02312-4

DOI: https://doi.org/10.1016/j.colsurfa.2024.135448

Reference: COLSUA135448

To appear in: *Colloids and Surfaces A: Physicochemical and Engineering Aspects*

Received date: 29 July 2024
Revised date: 23 September 2024
Accepted date: 25 September 2024

Please cite this article as: Thi Tuyen Nguyen, Rémi Marsac, Alexis Groleau, Jaimy Scaria and Yann Sivry, Binding Mechanisms of Trivalent Chromium on Colloidal Phases from Ultramafic Systems: Insights from Batch Experiments and XAS Analysis, *Colloids and Surfaces A: Physicochemical and Engineering Aspects,* (2024) doi:https://doi.org/10.1016/j.colsurfa.2024.135448

Binding Mechanisms of Trivalent Chromium on Colloidal Phases from Ultramafic Systems: Insights from Batch Experiments and XAS Analysis

Thi Tuyen Nguyen[1], Rémi Marsac[1*], Alexis Groleau[1], Jaimy Scaria[2], Yann Sivry[1]

[1] Université Paris Cité, Institut de physique du globe de Paris, CNRS, F-75005 Paris, France

[2] Univ Rennes, CNRS, Géosciences Rennes – UMR 6118, F-35000 Rennes, France

*Corresponding author: marsac@ipgp.fr

Graphical abstract

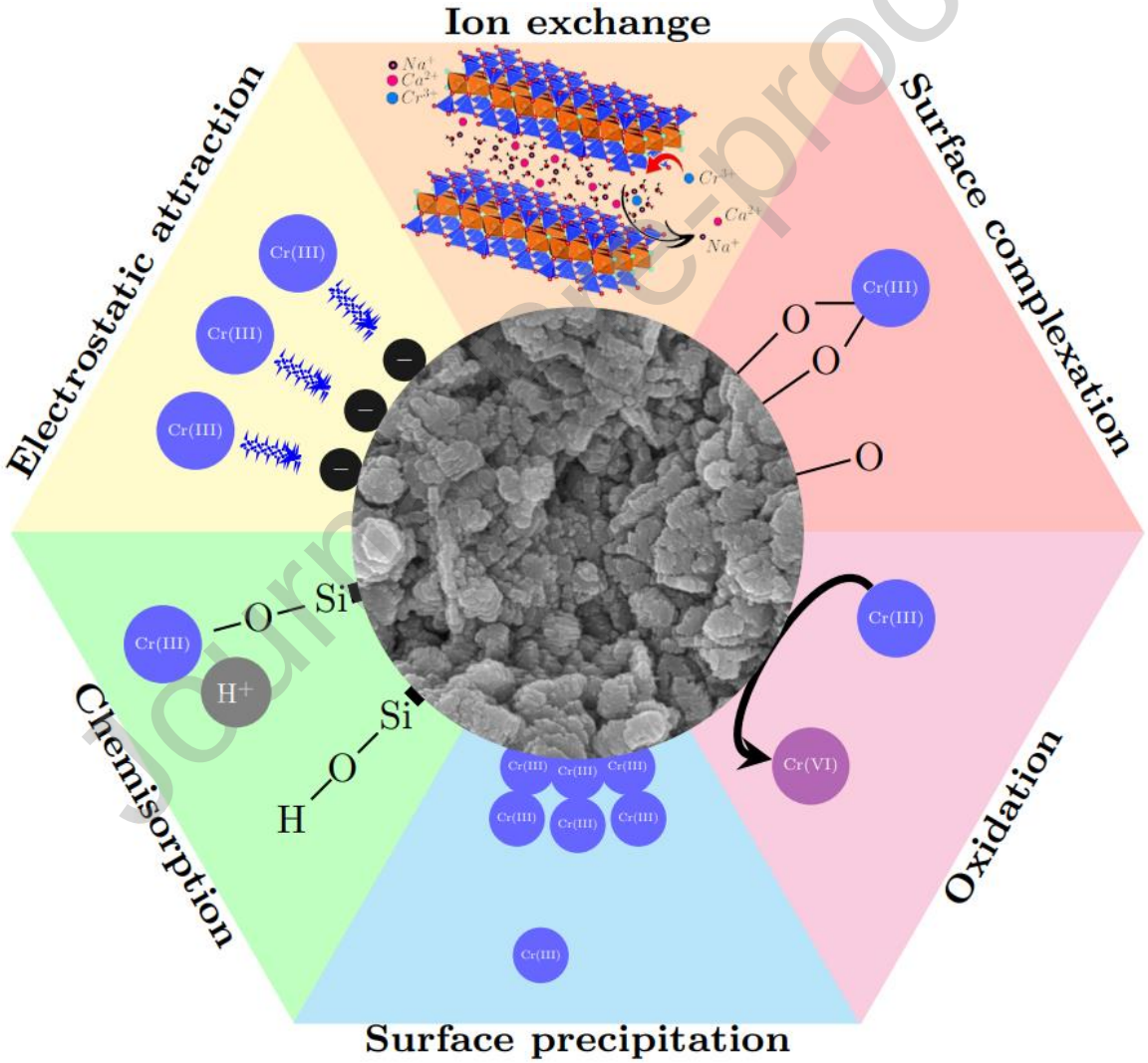

Abstract

Understanding the availability and mobility of chromium is a key factor in gaining insight into the fate of chromium and thus essential for assessing the risk of contamination and developing effective remediation strategies. In the natural environment, such as ultramafic systems, which are natural pools of chromium, chromium occurs mostly in the trivalent state (Cr(III)), which is known to have a high affinity for the solid phases such as particles and colloids. However, since Cr(VI) is more toxic, the vast majority of experimental studies focus on its reduction to Cr(III), which is often considered to form (hydr)oxide precipitates due to its poor solubility. Furthermore, while the oxidation state of Cr dictates its geochemical behavior, its interaction with particles and colloids is rarely controlled or monitored. Therefore, the interaction mechanisms between Cr(III) and particles or colloids require further attention. In this study, ten mineral phases (goethite, hematite, pyrolusite, kaolinite, montmorillonite, chlorite, serpentine, fuchsite, amphibole, and chromite) and one organic phase (humic acid), relevant to chromium bearing and carrier phases in ultramafic soils, were investigated to explore their interaction with Cr(III) species. These phases were first characterized by various techniques (including XRD, XRF, SEM, and BET). Adsorption and desorption experiments of Cr(III) on these phases were then carried out, and the distribution of Cr oxidation states in both the aqueous and solid phases was carefully monitored using UV-vis spectroscopy, geochemical speciation modeling, and Cr K-edge XAS spectroscopy. With the exception of pyrolusite, where partial oxidation of Cr(III) to Cr(VI) occurred, Cr(III) was shown to persist as a single oxidation state in all experiments. Desorption analyses showed significantly low desorbed rates, which further confirmed the prevalence of Cr(III). Experimental sorption isotherm data were interpreted using the Langmuir model and its linearized form, which provides important thermodynamic characteristics of adsorbents related to their structural and surface features. This study will provide better constraints for the understanding and prediction of Cr behavior and fate in the environment, especially in ultramafic systems.

Keywords: chromium, sorption, colloids, redox speciation

1. Introduction

Chromium (Cr) is considered as one of the most toxic elements which has caught worldwide attention due to its high threat to human health and ecosystems. Trivalent (Cr(III)) and hexavalent (Cr(VI)) forms are more stable and biologically relevant. While Cr(III) plays crucial roles in metabolic processes and is essential in trace amounts, Cr(VI) poses significant health risks and is the subject of regulatory concern due to its carcinogenic and toxic properties (Dayan and Paine, 2001; Namgung et al., 2014). Cr(VI) is highly soluble and mobile in aqueous environments, whereas Cr(III) tends to form insoluble precipitates or complexes, and is prone to adsorption onto solid surfaces such as soil particles and colloids (Oze et al., 2004). In nature, chromium is released into the environment from Cr-rich minerals in ultramafic environments such as chromite, serpentine mostly in the trivalent state via weathering processes. As the main geogenic source of Cr, ultramafic systems are associated with naturally enriched in high levels of Cr(III), which can pose significant environmental risks if released into the surrounding ecosystems. As a matter of fact, Cr(III) requires careful consideration due to its prevalence in natural environments and potential for long-term environmental persistence.

Once released, chromium species can be readily adsorbed by soil colloids such as iron oxides, manganese oxides, clays or organic matter (OM). These components act as scavengers or carrier phases (Choppala et al., 2013; Chrysochoou et al., 2016; Fendorf, 1995; Raous et al., 2013), which play a key role in the availability and mobility of chromium (Bolaños-Benítez et al., 2018; Quantin et al., 2021) in the environment, and hence in its toxicity (Aharchaou et al., 2017; Monga et al., 2022). According to Miranda et al. (2022), the major mechanisms driving heavy metals interaction with suspended particulate matter and sediment are sorption processes. They play a crucial role in regulating the availability and mobility of heavy metals in natural settings. Consequently, it is essential to understand the sorption characteristics of chromium species onto the Cr-carrying phases in order to predict Cr speciation, behavior and fate in natural settings. Nevertheless, doing this task is challenging due to the redox speciation of chromium. Indeed, master species of Cr(III) and Cr(VI) are, respectively, cationic (Cr^{3+}) and anionic (CrO_4^{2-}), whose interaction mechanisms with particles and colloids surfaces, and related adsorption behaviors, drastically differ (Hao et al., 2022; Oze et al., 2004). It was previously shown that, in order to predict the overall adsorption of a redox sensitive element, the adsorption behavior for each oxidation state must be known independently (Banik et al., 2017; Marsac et al., 2024; Ratié et al., 2023), as adsorption processes (e.g., surface complexation, ion exchange, surface precipitation) play a key role on the surface redox speciation (Marsac et al., 2024). There are various researches on the sorption of Cr(VI): Johnston and Chrysochoou, 2012; Kar and Equeenuddin, 2019; Zachara et al. 1988; Zhang et al. 2019 onto different carrying phases. In principle, the independent adsorption behavior of Cr(VI) should be known, because its

investigation is technically facilitated by its stability in oxidizing conditions. By contrast, if data are available for Cr(III) as initial reactant (e.g., Koppelman et al., 1980; Miranda et al., 2022; Seif et al., 2019; Sun et al., 2006), their relevance for the evaluation of Cr(III) adsorption behavior is questionable. Indeed, when examining the interaction between Cr(III) and particle or colloidal phases, in many studies Cr redox speciation is not monitored or controlled, although experiments were conducted under ambient atmosphere. Alternatively, experiments under anaerobic conditions with Cr(III) are scarce (Aiken et al., 2023). Therefore, it is not possible to state whether available data with Cr(III) as initial reactant are finally a mixture of Cr(III) and Cr(VI) or if they can directly be taken as independent adsorption data for Cr(III). In addition, most studies focus on conditions far from those typically encountered in natural soils, sediments and natural water. For example, they dealt with very high concentrations of chromium in order to develop innovative strategies for the remediation of highly contaminated areas (Covelo et al., 2007; Dzieniszewska et al., 2020; Sun et al., 2006). In such conditions, removal mechanism of Cr(III) from solution is surface precipitation (Hao et al., 2022), which might not be the relevant mechanism in many environmental conditions, such as in natural soils and waters (Aiken et al., 2023; Seif et al., 2019).

In order to fill these important gaps in the literature, namely the lack of data involving only Cr(III) at relatively low levels relevant to many natural systems, this study focuses on the sorption processes of trivalent chromium on a selection of inorganic and organic colloids. The final oxidation state of Cr was established both on the solid phase by X-ray Absorption Near Edge Structure (XANES) spectroscopy, and in solution by UV-vis absorption spectroscopy. Ten mineral phases (goethite, hematite, pyrolusite, chromite, amphibole, fuchsite, serpentine, chlorite, kaolinite, montmorillonite) and one organic phase (humic acid, HA), which are the most common (and stable) components of soils in the ultramafic environments, were selected as carrying phases. They were characterized by different techniques including X-ray diffraction (XRD), X-ray fluorescence (XRF), scanning electron microscopy (SEM), Brunauer-Emmett-Teller surface area analysis (BET), and the pH of zero point of charge (PZC) was determined for each phase. The sorption characteristics were deduced from the model fitting of experimental isotherms and by Extended X-ray Absorption Fine Structure (EXAFS) spectroscopy. Sorption isotherms experiments were conducted in physico-chemical conditions similar to the natural ultramafic systems (Becquer et al., 2003; Garnier et al., 2021; Oze et al., 2004). Therefore, present results may provide important data for the evaluation of Cr adsorption under the reducing conditions that can occur in various subsurface environments.

2. Material and methods

2.1. Reagents

All chemicals used, which were purchased from Sigma-Aldrich and Thermo Fisher Scientific, were of analytical grade. "Milli-Q" ultrapure water (specific resistivity of 18.2 MΩ.cm) was used to prepare the samples. The references $CrCl_3.6H_2O$ and K_2CrO_4 were also purchased from Sigma-Aldrich. The origin and general information of colloidal bearing phases are presented in full details in Table 1.

2.2. Materials

Goethite (FeOOH) was synthesized using the protocol developed by (Hiemstra et al., 1989). Hematite (Fe_2O_3) was purchased from US Research Nanomaterials, Inc. Pyrolusite (β-MnO_2) was purchased commercially from Thermo Scientific, American Kaolinite ($Al_2Si_2O_5(OH)_4$) and Montmorillonite ($(Na,Ca)_{0,3}(Al,Mg)_2Si_4O_{10}(OH)_2 \cdot nH_2O$) were provided by the Clay Society (American) (https://www.clays.org/sourceclays_data/). Chlorite ($(Mg,Fe)_5Al(Si_3Al)O_{10}(OH)_8$) was purified from natural sample originating from a lateric profile located in Barro Alto ultramafic massif, Brazil (S15°4' - E48°584'), by Dithionite-Citrate-Bicarbonate (DCB) according to Holmgren, 1967 to remove iron oxides (Zelano et al., 2016). Serpentine ($Mg_3Si_2O_5(OH)_4$) was collected from serpentine rocks originating from southwestern France, and was provided by the Muséum National d'Histoire Naturelle de Paris (MNHN). Chromite ($FeCr_2O_4$), Amphibole ($Ca_2(Mg_5Fe)(Si_8O_{22})(OH)_2$), and Fuchsite ($K(Al,Cr)_2(AlSi_3O_{10})(OH)_2$) were separated manually from chromite ore sample, from Sittampundi, Tamil Nadu, India (N 11° 13' - E77° 56', under a stereomicroscope. HA, purchased commercially (Thermo Scientific, American), was purified following the protocol for Humic substances (IHSS) (humic-substances.org).

2.3. Characterization of the mineral and organic phases

The mineralogical composition of the mineral phases was determined by the X-ray diffraction (XRD) technique using the PANalytical Empyrean diffractometer with Cu Kα radiation (at 40kV 40mA). The diffractometer is equipped with multi-channel detectors. X-Ray fluorescence (XRF) analysis was used to determine the elemental content of the solid phases using Panalytical Minipal 4 (Rh X-Ray tube – 30KV-9W) at a resolution of 150 eV (Mn Kα). The information on the elemental composition of the solid phases is encoded in Backscattered electron images, which were obtained using a Philips XL30 scanning electron microscope (SEM) operating at 15kV beam voltage and 1.5µA beam current. The specific surface area

(SSA) is determined experimentally using the BET method, using a Belsorp-max apparatus from MicrotracBEL. The samples were outgassed for 12 hours at 150 °C and 0.1 Pa prior to analysis. The BET treatment was performed in the relative pressure range of 0.05 to 0.25. This range was recommended by IUPAC for the BET analysis for a precise surface area measurement (Elmaalouf et al., 2021; Thommes et al., 2015). The pH drift method was adopted to determine the pH of point zero charge (PZC) of the mineral and organic phases (Smičiklas et al., 2000). Initial pH (pH_i) values of the solutions containing 25 mL of 0.1M $NaNO_3$ and 0.1 g for each solid were adjusted in the range from 2 to 10 using the HCl or NaOH solution (0.1 M and 1 M). The sample was kept on an end - over - end shaker at 250 rpm and 25°C ± 1°C for 24 h. The final pH (pH_f) values of the solutions were measured by an ORION STAR A111 pH-meter, calibrated with pH buffer solutions. The PZC was determined from a plot of (pH_i - pH_f) versus pH_i.

2.4. Adsorption experiments

A 100 mg L^{-1} Cr(III) stock solution was prepared by dissolving chromium chloride ($CrCl_3.6H_2O$) in distilled water. The Cr(III) adsorption experiment was carried out in a supporting electrolyte concentration and pH value of 5, typical for ultramafic soils (Becquer et al., 2003; Garnier et al., 2021) (0.4 mM $CaCl_2$ and 0.6mM $NaHCO_3$, ionic strength I = 1.87 mmol L^{-1}) and which was adjusted using 0.1 M NaOH or 0.1 M HCl solution. The solid phase content in the solution was 1 g L^{-1} and total Cr(III) concentrations (C_0) were set to 0.1, 0.2, 0.3, 0.4, 0.5, 0.6, 0.7, 0.8, 0.9, 1.0, 1.3, 1.7, 2.0 or 2.5 mg L^{-1}. Samples for the Cr(III) concentrations of 0.1, 0.5, and 0.9 mg L^{-1} were prepared in triplicate. HA was dissolved at pH 13 by 1M NaOH before the adsorption experiment. To avoid the possible microorganism development during the experiment, 10 µL of a 1 M sodium azide (NaN_3) solution was added to each tube. The tubes were then put in an end-over-end shaker at a rate of 80 rpm at 25 °C in 2 months for the concentration 2.0 mg L^{-1}, and in 72 h for the remaining concentrations.

During reaction, the pH values of the solutions were verified and adjusted to 5 if necessary. After the given reaction times, a certain amount of solution from each tube is withdrawn for the adsorption measurement. The remainder is kept for the subsequent experiment, which is either desorption or XANES analyses. On each sample, the supernatant was passed through a 0.02 µm Anotop syringe filter (or 1 kDa MWCO ultracells for HA) and the final aqueous Cr(III) concentration C_e was measured by an Inductively Coupled Plasma Optical Emission Spectroscopy (ICP-OES) (Spectrogreen, AMETEK). The spectrometer can measure elemental

concentrations down to 4 µg L^{-1}, therefore it could be used for trace elements including chromium.

A 1.5 diphenyl carbazide (DPC) colorimetric assay was employed to quantify Cr(VI), as previously described by (Bartlett and James, 1979). To prepare the DPC reagent, 0.05 g of DPC was dissolved in 10 mL of methanol, the obtained solution was then added into 87.2 mL of double deionized water with 2.8 mL of H_2SO_4, limiting light exposure.

For an accurate interpretation of the adsorption data, it is crucial to know whether Cr(III) actually retains and prevails on the surface of the adsorbents, as partial oxidation of Cr(III) to Cr(VI) cannot be excluded in the presence of oxygen *a priori* (Guo et al., 2024; Liang et al., 2021). This speciation analysis must be done both for the solution and the solid phase because Cr(III) and Cr(VI) ions can fractionnate between both these compartments (Marsac et al., 2024). To determine Cr(VI), 0.125 mL of the DPC reagent was mixed with 1 mL of the filtered sample and left for 20 minutes. The Cr(VI) concentration of samples was then determined using the UV-Vis spectrophotometer at 540 nm with a detection limit of 5 µg L^{-1}. For samples conditioned at [Cr] = 2 mg L^{-1}, the remaining suspensions were kept for the XAS analysis, which allows to determine the redox speciation of Cr in the solid phase. The suspensions were centrifuged at 5000 rpm in 10 min, and then, the supernatant was removed. The solids were washed with the deionized water to get rid of the residual chromium, then freeze-dried and prepared for the XANES analysis.

Adsorption densities Q_e (in µg m^{-2}) of the Cr(III) were calculated according to the following formulae (Alsaiari et al., 2021):

$$Q_e = \frac{(C_0 - C_e)}{SSA \times m_{solid}} \times V \quad (1)$$

where C_0 and C_e (in µg L^{-1}) are the concentrations at the initial point and at the equilibrium, respectively; SSA ($m^2\ g^{-1}$) is the specific surface area of the minerals, m_{solid} (g) is the mass of the solid adsorbent, and V (L) is volume of the solution.

2.5. Desorption experiments

Desorption experiment of Cr(III) was carried out after the adsorption process on the remaining samples at concentrations (0.1, 0.3, 0.5, 0.7, 1.0 mg L^{-1}). The solutions were centrifuged to

remove the supernatant. The centrifuged solids were then washed with some drops of ethanol (absolute, 96%) to remove the trapped metal solution. They were dried overnight in an oven at 40°C and then were weighed to measure the amount of retained mass of solid. The same volume of the background solution (0.4 mM $CaCl_2$ and 0.6 mM $NaHCO_3$) was added and adjusted to pH 5 using 0.1 M NaOH or HCl, and the mixtures were stirred at 80 rpm in an end-over-end shaker for 24 h. The 24 h equilibration time was established by previous study (Gunawardana et al., 2013). The solution was filtered through a 0.02 µm syringe filter and acidified to HNO_3 2%. The filtrates were stored in the fridge before measurement. The concentration of Cr(III) was measured by a Quadrupolar Inductively Coupled Plasma Spectroscopy (QICPMS, 7900 Agilent). This spectrometer can measure chromium concentrations ranging from 0.1 to 200 µg L^{-1}, with a detection limit of 0.04 µg L^{-1} for Cr.

The desorption percentage is calculated as follows (Bayuo et al., 2020):

$$\%desorption = \frac{m_{desorbed}}{m_{adsorbed}} \times 100 \qquad (2)$$

2.6. X-ray Absorption Spectroscopy

The chemical speciation of chromium adsorbed on the surface of mineral and organic phases was done using the Cr K-edge XANES, at the LUCIA beamline of the synchrotron SOLEIL (Flank et al., 2006; Vantelon et al., 2016). The samples were prepared as pellets of finely crushed and homogenized powder mixed with cellulose. The XANES spectra of K_2CrO_4 and $Cr(OH)_3$, were also recorded and utilized as the references for their known oxidation states of chromium. The X-ray beam was monochromatized using a Si (111) double-crystal monochromator. The monochromator was calibrated by setting the first inflection point of a Cr metallic foil XANES spectrum to 5987 eV. Spectra were collected in fluorescence mode (using a Bruker 60 mm^2 mono-element SDD). XANES spectra were collected with a beam size of 2×2 mm^2 under a secondary vacuum (10^{-7} mbar), at room temperature. These measurements were conducted using the XANES "e-flyscan" continuous mode on the LUCIA beamline, over an energy range from 5950 eV to 6080 eV, with the energy step of 0.4 eV. The counting duration was 300 ms per point. The recorded spectra (up to ten) were superimposed for each sample, demonstrating that no beam damage occurred during measurements, and then merged. The XANES spectra were aligned, combined, and processed using the FASTOSH software (Landrot, 2018). Normalized spectra were obtained by fitting the pre-edge region with a linear

function and the post-edge region with a quadratic polynomial function. For detailed structural analysis, Extended X-ray Absorption Fine Structure (EXAFS) was conducted. EXAFS oscillations were extracted using the Autobk algorithm with a cut-off Rbkg = 1 and k-weight = 2. The EXAFS spectra were converted from energy to R-space, achieving Fourier transform (FT) spectra as a function of $k^2\chi(k)$ with the hanning window in the range 3 - 10.5 $Å^{-1}$. Phase shifts and amplitudes for relevant backscattering were calculated using FEFF 7 and WinXAS (Ankudinov et al., 1998). For modeling of the EXAFS spectra, the Artemis software (Ravel and Newville, 2005) from the Demeter package was employed, incorporating various weighting schemes (k^1-, k^2-, and k^3-weighting) (García-Guaderrama et al., 2015) to determine the the coordination number (N), interatomic distance (R) and the Debye−Waller value (σ^2). Shell by shell fitting with theoretical standards was performed, where the optimal fits for the first shell (Cr-O) were subsequently fixed for higher shell fitting.

2.7. Geochemical speciation modeling

Aqueous chemical speciation calculations were performed using PhreePlot (Kinniburgh and Cooper, 2011), which contains an embedded version of the geochemical speciation program PHREEQC (Parkhurst and Appelo, 1999). The "Minteq.v4.dat" database was used for the calculations. Ionic strength effects on equilibrium constants were calculated using the Davies equation.

3. Results and discussions

3.1. Mineral characterization

XRD and XRF results

The characterization results of the mineral phases are reported in Figure S1 and Table 1. XRD results suggest high purity (100%) of goethite, hematite and pyrolusite samples. XRF results consistently show that Fe is the dominant component of goethite and hematite, while it is Mn in the case of pyrolusite. As oxides, they account for more than 80% of the total composition of the corresponding phase. For goethite, Al and Si are found by XRF as minor components. The presence of Al can be explained by a partial substitution of Fe(III) by Al(III) in the crystal lattice, without significantly affecting goethite purity. In addition, Si can be present in goethite

between crystal domains, and hence, does not modify the crystal structure (Glasauer et al., 1999).

The principle components (well above 1%) of kaolinite, montmorillonite, and fuchsite are multifold: they are oxides of Al and Si for kaolinite, and of Mg, Al, Si for montmorillonite, and Al, Si and K for fuchsite. For each of the five above phases, the dominant elements are relevant to its intrinsic composition, while others are very minor (approximately or less than 1%). This fact suggests the relatively good purity of these phases. This is further confirmed by XRD analysis: their diffractograms contain only their own corresponding characteristic peaks, consistent with a high purity of these phases (100%).

The other phases also contain significant proportions of other metals besides the main intrinsic elements. However, unlike goethite, the XRD analysis shows that they are mixed, highlighting that there are several phases coexisting in their structure. For chlorite, they are clinochlore ($Mg_5Al(AlSi_3O_{10})(OH)_8$: 80%) and quartz ($SiO_2$: 20%). In these two phases, quartz is considered a relatively non-reactive surface (Ali et al., 2021), so it would actually have a minor role in the sorption reactions. Concerning the two remaining phases, the serpentine is a mixture of lizardite ($Mg_3(Si_2O_5)(OH)_4$: 47%), brucite ($Mg(OH)_2$: 43%), and magnetite ($Fe^{2+}Fe_2^{3+}O_4$: 10%), while chromite consists of chromite ($FeCr_2O_4$: 79%), birnessite (δ-MnO_2: 6%), bixbyite ($(Mn,Fe)_2O_3$: 3%) and quartz (SiO_2: 12%). The amphibole was shown to be a mixture of two coexisting phases: the pargasite ($NaCa_2(Mg_4Al)(Si_6Al_2)O_{22}(OH)_2$: 90%) and the clinochlore ($(Mg,Fe^{2+})_5Al(Si_3Al)O_{10}(OH)_8$: 10%).

Table 1. Characterization of the mineral phases. LOI: Loss On Ignition

		Goethite	Hematite	Pyrolusite	Kaolinite	Montmorillonite	Chlorite	Serpentine	Fuchsite	Chromite	Amphibole
XRF (%)	Na_2O	0.06	0.42	-	0.62	0.33	0.98	0.56	0.81	0.22	0.73
	MgO	0.02	-	-	0.28	2.81	13.46	45.93	1.28	11.32	18.87
	Al_2O_3	2.12	-	0.02	26.71	13.36	20.93	-	36.74	25.70	12.00
	SiO_2	3.80	0.18	-	51.00	66.30	37.94	19.03	47.40	3.22	44.80
	P_2O_5	0.21	0.07	0.06	-	0.04	0.06	0.06	0.07	0.05	0.03
	K_2O	0.02	-	-	1.39	0.11	-	-	9.03	-	-
	CaO	0.04	0.11	0.04	0.57	1.68	0.07	0.09	0.07	1.07	11.56
	TiO_2	-	0.14	-	-	0.20	0.12	0.02	1.58	0.26	1.58
	MnO	-	0.06	84.03	-	0.01	0.55	0.07	0.02	2.75	0.27
	Fe_2O_3	82.6	96.24	0.60	0.37	1.07	11.90	26.06	0.31	20.00	6.22
	Cr_2O_3	-	-	-	-	-	-	-	-	34.16	-
	LOI	8.86	2.78	15.26	15.20	14.06	13.96	8.18	2.70	1.26	3.94
Cr detected by SEM-EDX		No	No	No	No	No	Yes	No	Yes	Yes	Yes
XRD (semi-quantitative)		100%	100%	100%	100%	100%	clinoclore (80%), quartz (20%)	lizardite (47%), brucite (43%), magnetite (10%)	100%	chromite (79%), birnessite (6%), bixbyite (3%), quartz (12%)	pargasite (90%), clinochlore (10%)
Particle size		100 - 500 nm	100 - 200 nm	10 - 25 µm	50 - 100 nm	0.1 - 2 µm	1 - 50 µm	1 - 50 µm	50 - 300 µm	50 - 300 µm	10 - 300 µm
SSA ($m^2 g^{-1}$)		86.2	13	1.69	19.3	92.5	16.5	13.3	0.60	0.64	1.18
PZC		7.03	4.78	3.52	4.29	6.99	4.86	8.88	6.21	6.75	9.57

SEM observations and specific surface areas

The SEM images and the BET measurement of different solid phases are shown in Figure 1 and Table 1. These two analyses are somehow related, as the smallness of the grain size from SEM usually implies the largeness of the SSA. Goethite crystals are needle-shaped (Figure 1a) and may vary considerably in size, which is consistent with the literature (see Kosmulski et al., 2004). A majority of the needles are 10–20 nm wide and 100–500 nm long in size. Concerning the BET measurement, the SSA is 86.2 $m^2 g^{-1}$. This result is in good agreement with the reported values in the literature (such as Guo et al., 2009; Ratié et al., 2023; Weerasooriya and Tobschall, 2000). Hematite crystals have plate-like morphology, and are 100-200 nm in size (Figure 1b). The measured SSA value is 13 $m^2 g^{-1}$, which is close to the value of 17 $m^2 g^{-1}$ reported in Ko et al. (2005), for instance. The SEM image of pyrolusite (Figure 1c) shows its highly-aggregated and spherical-shaped structure of size 10-25 µm. The SSA of pyrolusite is estimated to be 1.69 $m^2 g^{-1}$, which is in the same order of magnitude as the reported values from Aiken et al. (2023) (6.23 $m^2 g^{-1}$) and Islam et al. (2020) (4.8 $m^2 g^{-1}$). Kaolinite (Figure 1d) and montmorillonite (Figure 1e) have a layered structure. The hexagonal-like crystalline particles of the former are

typically about 200 nm to 400 nm. Its measured SSA is 19.3 $m^2 g^{-1}$, which is comparable to the value reported by Rao et al. (2012) (24.58 $m^2 g^{-1}$). For montmorillonite, the particle size ranges from 100 nm to 2 μm, and its SSA value is estimated to be 92.5 $m^2 g^{-1}$. This is similar to the value given by Zhu et al. (2018). As shown in Appendix (Figure S2), chlorite, serpentine, fuchsite, chromite, and amphibole were very aggregated and it was difficult to determine the size of the primary particles by SEM. Chlorite (Figure S2a) has an SSA value of 16.5 $m^2 g^{-1}$, which is similar to the reported values of Koppelman et al. (1980). Serpentine (Figure S2b) has a SSA of 13.3 $m^2 g^{-1}$. Fuchsite (Figure S2c), chromite (Figure S2d), and amphibole (Figure S2e), exhibit SSA values around 1.0 $m^2 g^{-1}$ (see Table 1).

(a) Goethite

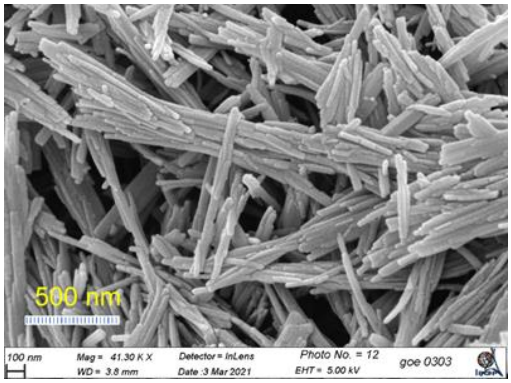

(b) Hematite

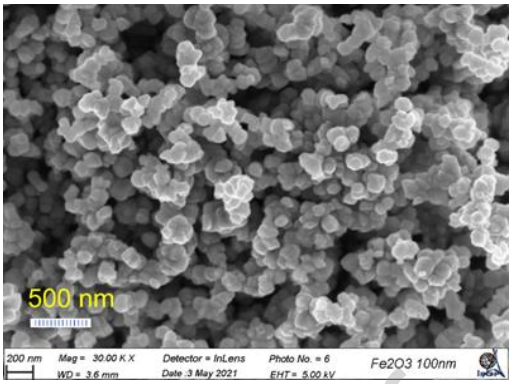

(c) Pyrolusite

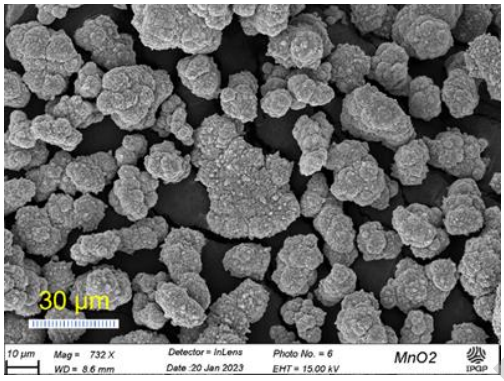

(d) Kaolinite

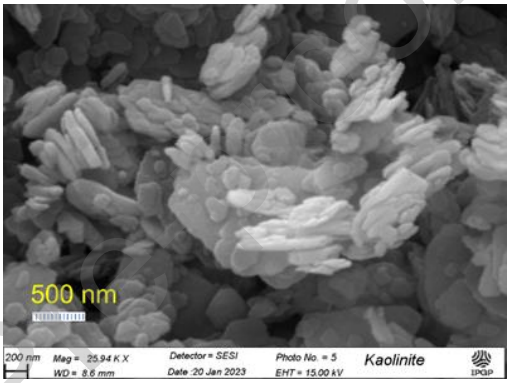

(e) Montmorillonite

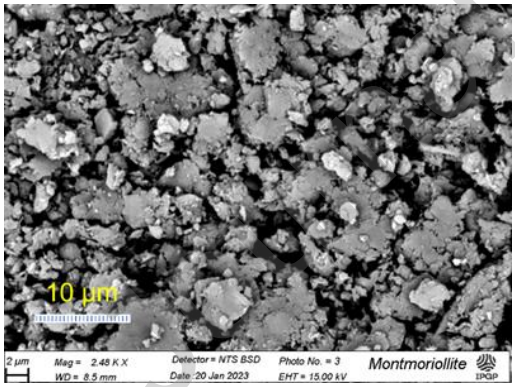

Figure 1. SEM images of (a) goethite, (b) hematite, (c) pyrolusite, (d) kaolinite, (e) montmorillonite.

Point of zero charge (PZC)

The pH of the system controls the adsorption capacity due to its influence on the surface properties of the adsorbent, and on the ionic forms of chromium in solution. Table 1 shows the point of zero charge (PZC) of the 10 mineral phases (titration data are provided in Figure S3). The PZC values obtained for solid phases in the current study read: goethite (7.0), hematite (4.78), kaolinite (4.29), montmorillonite (6.99), chlorite (4.86), serpentine (8.88), and chromite

(6.75). In general, the PZC values from they are in good agreement with the corresponding values from previous studies: Ugbe and Abdus-Salam (2018) (goethite: 7.0), Vieira et al. (2011) (hematite: 4.43), Singh and Mackinnon (1996) (kaolinite: 4.5), and Veselská et al. (2016) (kaolinite: 4.13), Bourg et al. (2007) (montmorillonite: 7.0), Alvarez-Silva et al. (2010) (chlorite: 4.7), Feng et al. (2012) (serpentine: 10.2), Souza et al. (2012) (chromite: 6.5). For pyrolusite, our finding is 3.52, which lies in the range 2.5-5.8 from the literature (Bernard et al., 1997; Gheju et al., 2016). Because the Cr adsorption experiments were conducted at the pH value of 5, one can divide the considered phases into two distinct groups: (i) minerals with a mostly negative surface charge, including hematite, pyrolusite, kaolinite, and chlorite; and (ii) minerals having a principally positively charged surface, involving goethite, montmorillonite, serpentine, amphibole, fuchsite, and chromite.

3.2. Cr redox speciation analysis in the aqueous and solid phases

UV-vis spectroscopy was used to quantify [Cr(VI)] in solution, and XANES was used to probe Cr redox speciation at the surface of the solids. In addition, geochemical speciation modeling was used to determine the prevailing dissolved species, whereas further information regarding the Cr surface speciation were obtained by EXAFS data analysis. In order to achieve reliable spectroscopic data, corresponding batch adsorption experiments were conducted for [Cr] = 2 mg L^{-1}. Table S1 shows that all mineral phases can adsorb Cr strongly at such concentration, as about 55% to 92% of Cr was removed from the solution. As a result, final Cr aqueous concentration ranges from 0.15 to 0.9 mg L^{-1}. Finally, the retention of Cr(III) on the surface of the adsorbent was assessed using the desorption analysis.

Cr speciation in the aqueous phase

For all phases other than pyrolusite, no Cr(VI) was detected with UV-vis spectroscopy. Given the detection limit of 5 µg L^{-1} of this technique, one can assume that it represents less than 3% of the final aqueous Cr concentration. With pyrolusite, 20.14 µg L^{-1} of dissolved Cr(VI) was detected in the solution, which corresponds to only 4% of the final aqueous Cr concentration (i.e. 1% of the total Cr(III) amount initially added to the suspension). Aqueous speciation calculations were performed for [Cr] = 2 mg L^{-1} (Figure 2). As we focus on a comparison with experimental results of dissolved Cr, no precipitation was considered in the calculations. Modeling results show that Cr(VI) is supposed to prevail under ambient atmosphere (i.e. 0.21 atm $O_{2(g)}$) but, as its stability field is rather narrow at pH 5, Cr(III) might persist over sufficiently

long time to prevail in the present experimental conditions. In addition, Figure 2 shows that $CrOH^{2+}$ is the prevailing Cr(III) species in solution at pH 5.

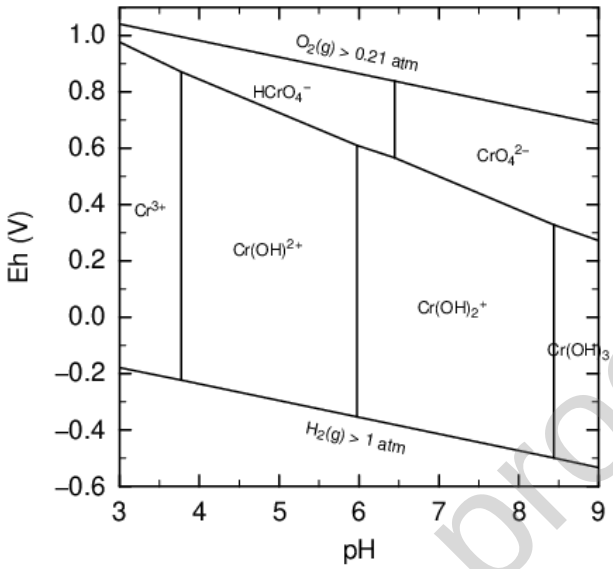

Figure 2. Predominance pH-Eh (Pourbaix) diagram of Cr obtained using Phreeplot (2 mg L^{-1} Cr, 0.4 mM $CaCl_2$, 0.6 mM $NaHCO_3$).

Cr species identification on the solid phase using XAS

Cr K-edge XANES spectra of the references as well as of the seven Cr(III) - adsorbed mineral and organic phases (HA, goethite, hematite, serpentine, kaolinite, montmorillonite, and pyrolusite) are shown in Figure 3. They are compared with reference spectra of K_2CrO_4, which exhibits an intense prepeak at 5993.5 eV characteristic of Cr(VI) in tetrahedral environment, and $Cr(OH)_3$, which exhibits a small prepeak at 5991.5 eV and a maximum intensity of the white line (WL) at ~6009.5 eV. In $Cr(OH)_3$, Cr(III) occurs in octahedral symmetry and shares edges with its neighbors (Papassiopi et al., 2014). Because chlorite, fuchsite, amphibole, and chromite contain structural Cr (Table 1), XANES data cannot be used to elucidate Cr surface speciation. Instead, chromite XANES spectrum is shown as a reference sample of Cr(III) in spinel structure, which differs from that of $Cr(OH)_3$ by the stronger intensity of its WL. Except for pyrolusite, the spectral shape of Cr bound to all phases conforms with the one of the reference $Cr(OH)_3$, with (i) the absence of the prepeak at 5993.5 eV, (ii) a white line (WL) at ~6009.5 eV and (ii) a relatively weak WL intensity compared to chromite. The XANES spectra indicate that Cr(III) prevails at the surface of all these adsorbents, and, except for pyrolusite, the adsorbed Cr(III) persisted without turning into Cr(VI) during the adsorption.

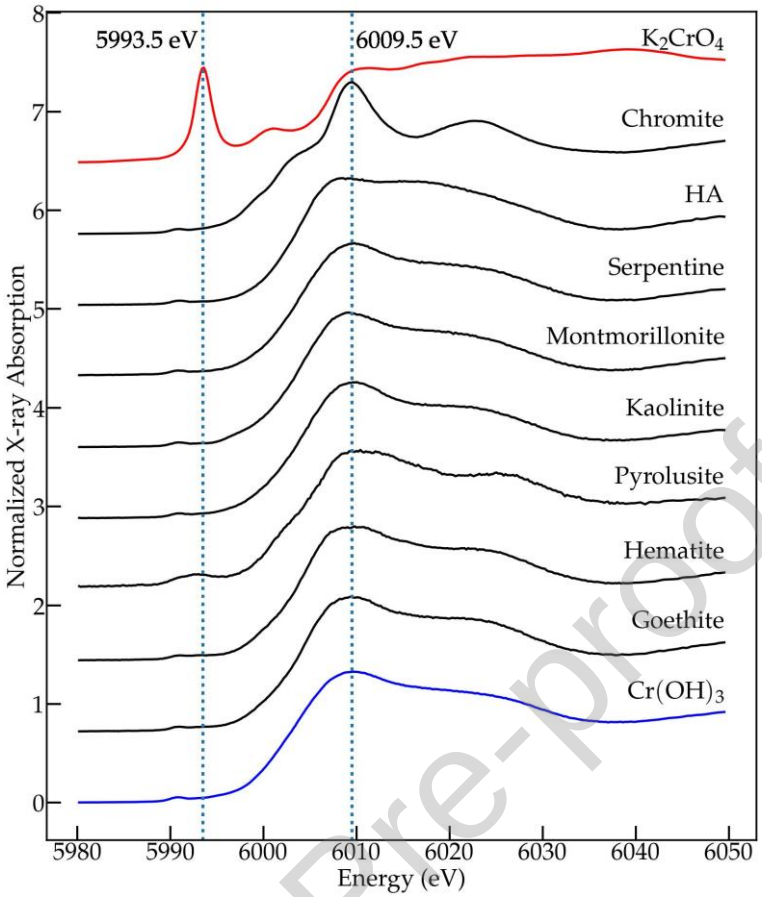

Figure 3. XANES spectra of Cr(III) adsorbed onto different phases

For pyrolusite, there is a small peak of Cr(VI) at about 5993.5 eV in the spectrum in addition to the dominant peak of Cr(III), which suggests the presence of the former in small amounts. The linear combination fits (LCF) of Cr references XANES show that Cr(VI) amounts to about 10% of the total adsorbed chromium, which resulted from the oxidation of Cr(III). This result is consistent with the occurrence of Cr(VI) in solution. The occurrence of this oxidation is justifiable, since pyrolusite serves as an end-member case for Mn(IV)-driven oxidation group (Schaefer et al., 2017). In addition, Apte et al. (2006) found that, in the presence of MnO_2, $Cr(OH)_3$ was progressively converted to dissolved Cr(VI) with low conversion rates, up to 1% in 60 days. Furthermore, the adsorption of Cr(VI) on pyrolusite is unfavorable at pH values greater than PZC due to the electrostatic repulsion between the Cr(VI) oxyanion and the negatively charged surface of pyrolusite at pH = 5. These facts explain the small amount of Cr(VI), together with its appearance in the solution. It is interesting to note that this result is similar to that of Aiken et al. (2023) who also found a small amount of Cr(VI) (18.72 µg L^{-1}) in the solution after the adsorption of Cr(III) on pyrolusite.

The EXAFS results and model fits are compared in Figure 4 and the structural parameters from EXAFS fitting are shown in Table 2. Only the systems where Cr(III) occurred as a single oxidation state, and where its surface speciation could be studied, were considered (i.e. hematite, goethite, serpentine, montmorillonite, kaolinite and HA). In all these samples, the first-shell analysis revealed that chromium exhibited coordination with 6 oxygen atoms. The Cr−O distances in the first coordination shell ranged from 1.97 to 1.98 Å, consistent with previous findings for hydrated and hydrolyzed Cr(III) ions and complexes (Chen et al., 2013), as well as present XANES data. Analysis of the higher coordination shells in Figure 4 demonstrated consistent variations in the coordination environment of Cr(III) based on the adsorbing material. Among iron oxides, the Cr(III) on hematite exhibited Cr-Fe/Cr paths at ~3.03 Å, in agreement with previous studies of Cr(III) adsorption onto hydrous ferric oxide (Charlet and Manceau, 1992). A bidentate edge-sharing inner-sphere surface complex formation can be expected based on geometrical considerations. Note that Cr or Fe in a second shell cannot be distinguished by EXAFS. However, for Cr(III) on goethite, no more distant neighbor than O were identified due to the low backscattering intensity. This might be due to the co-occurrence of several species onto the goethite surface. The local coordination environment of Cr(III) octahedra was found to be consistent among different clays under the experimental conditions. The second coordination shell composed of 2-3 Cr−Al/Si atoms at distances ranging from 2.78-2.82 Å, in line with previous analyses of Cr(III) adsorption to clay minerals or at the γ-Al_2O_3-Water Interface (Fitts et al., 2000; Hao et al., 2022). EXAFS analysis of Cr(III) bound to HA revealed a Cr−O distance at 1.97 Å is close to that obtained for the hydrated Cr sample or Cr(III)-bound to HA (Gustafsson et al., 2014). In addition, a second shell contains approximately two atoms at 3.32 Å, which we suspect to be attributed to polymeric species of Cr(III) bound to HA. Several species have been observed, characterized by Cr−Cr distance at approximately 2.99 Å and 3.5-3.6 Å (Gustafsson et al., 2014). While a Cr−Cr distance at 3.3-3.4 Å was not observed for Cr bound to HA yet, this was the case synthetic Cr(III) complexes (Vlachos et al., 2004) and for Fe(III), which has a similar behavior to Cr(III), with a Fe−Fe distance in the range 3.37-3.48 Å (Gustafsson et al., 2007; Mikutta and Kretzschmar, 2011).

Table 2. Fitting parameters of the EXAFS Spectra. a: N values were fixed at known values; *Estimated errors R and ΔE: values between brackets correspond to the error on the last digit. Estimated errors for σ^2 and CN: first shell (σ^2 ±10%), second shell (CN ±20%, σ^2 ± 30%); error represents 95% confidence interval.*

Sample	**Interaction**	***R* (Å)**	**CN**	**σ^2(Å^2)**	**ΔE/eV**	**R factor**
HA	Cr-O	1.97 (1)	6.0 [a]	0.003	-4.3 (2.5)	0.04
	Cr-Cr	3.32 (5)	1.9	0.010		
Serpentine	Cr-O	1.97(1)	6.0 [a]	0.003	-6.3 (1.9)	0.01
	Cr-Al/Si	2.78(2)	2.1	0.005		
Montmorillonite	Cr-O	1.97(1)	6.0 [a]	0.003	-2.8 (2.4)	0.02
	Cr- Al/Si	2.82(3)	2.9	0.011		
Kaolinite	Cr-O	1.97 (1)	6.0 [a]	0.003	-5.6 (2.5)	0.02
	Cr-Al/Si	2.80 (3)	2.4	0.008		
Hematite	Cr-O	1.98(1)	6.0[a]	0.003	-2.9 (2.8)	0.02
	Cr-Cr	3.03(3)	2.3	0.008		
Geothite	Cr-O	1.97(2)	6.0 [a]	0.003	-4.9 (3.2)	0.01

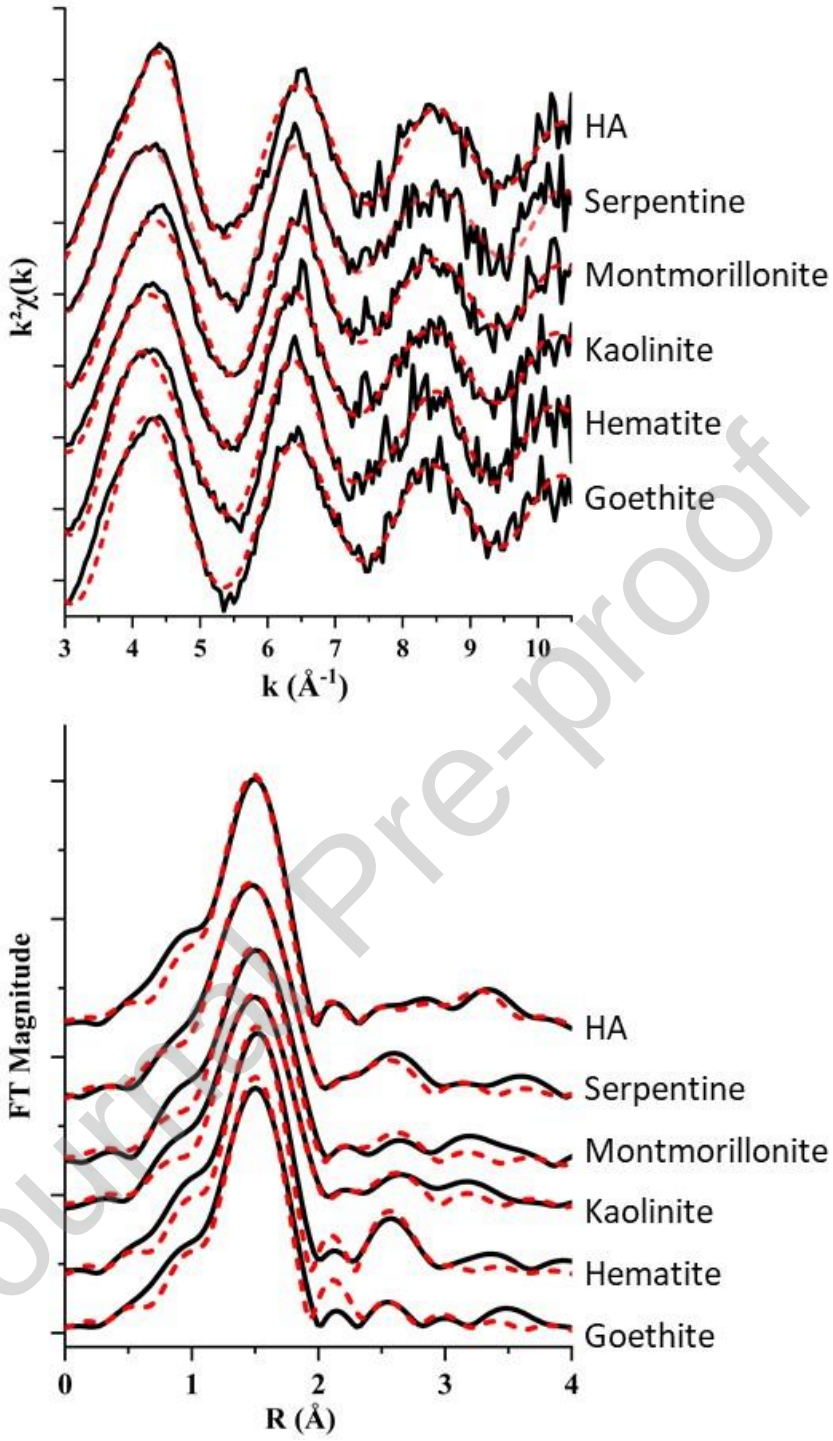

Figure 4. Stacked k^2-weighted Cr K-edge EXAFS spectra (a) and Fourier Transforms (b). Lines are raw data and dashed lines are best fits.

3.3. Sorption isotherm

The experimental isotherm data are shown in Figure 5. For all systems, the amount of adsorbed Cr(III) (Q_e) increases linearly with the final aqueous Cr(III) concentration (C_e), when C_e is sufficiently low. Based on the shape of the isotherm curves, they can be classified into two groups. For three phases (fuchsite, chromite, and HA), the isotherm remains linear within the range of experimental conditions investigated. However, for eight phases (goethite, hematite, pyrolusite, amphibole, serpentine, chlorite, kaolinite, and montmorillonite), a nonlinear adsorption behavior is observed at high C_e values, where adsorption data seem to tend to a plateau. Owing to this fact, Langmuir isotherm equation was chosen to describe the data, which assumes the monolayer adsorption onto a homogeneous surface:

$$Q_e = \frac{Q_{max} K_L C_e}{1 + K_L C_e} \qquad (3)$$

where Q_{max} (in mg m^{-2}) is the maximum adsorption capacity and K_L (in L mg^{-1}) is the Langmuir constant, which represents the strength of the adsorption onto the adsorbent surface (Do, 1998). At low C_e such that $K_L C_e \ll 1$, the Langmuir equation becomes linear, and hence, the following form is employed for the fitting exercise:

$$Q_e = Q_{max} K_L C_e \qquad (4)$$

In these conditions, it is not possible to distinguish Q_{max} and K_L by a fitting procedure. Instead, it is possible to determine K_d values (in L m^{-2}), which is related to the two parameters of the original Langmuir model as:

$$K_d = Q_{max} K_L \qquad (5)$$

Hence, K_d values were used to compare the two groups of adsorbents for which we observed linear or Langmuir-type adsorption isotherm for Cr. Note that, as it is difficult to determine the surface area of HA, K_d values are provided in L g^{-1} and will be discussed separately from the other phases. Results of the parameter fit with either equation 3 or 4 are shown in Figure 5, and optimized parameters are provided in Table 3. To compare all adsorbents, K_d values were also calculated using Langmuir equation parameters.

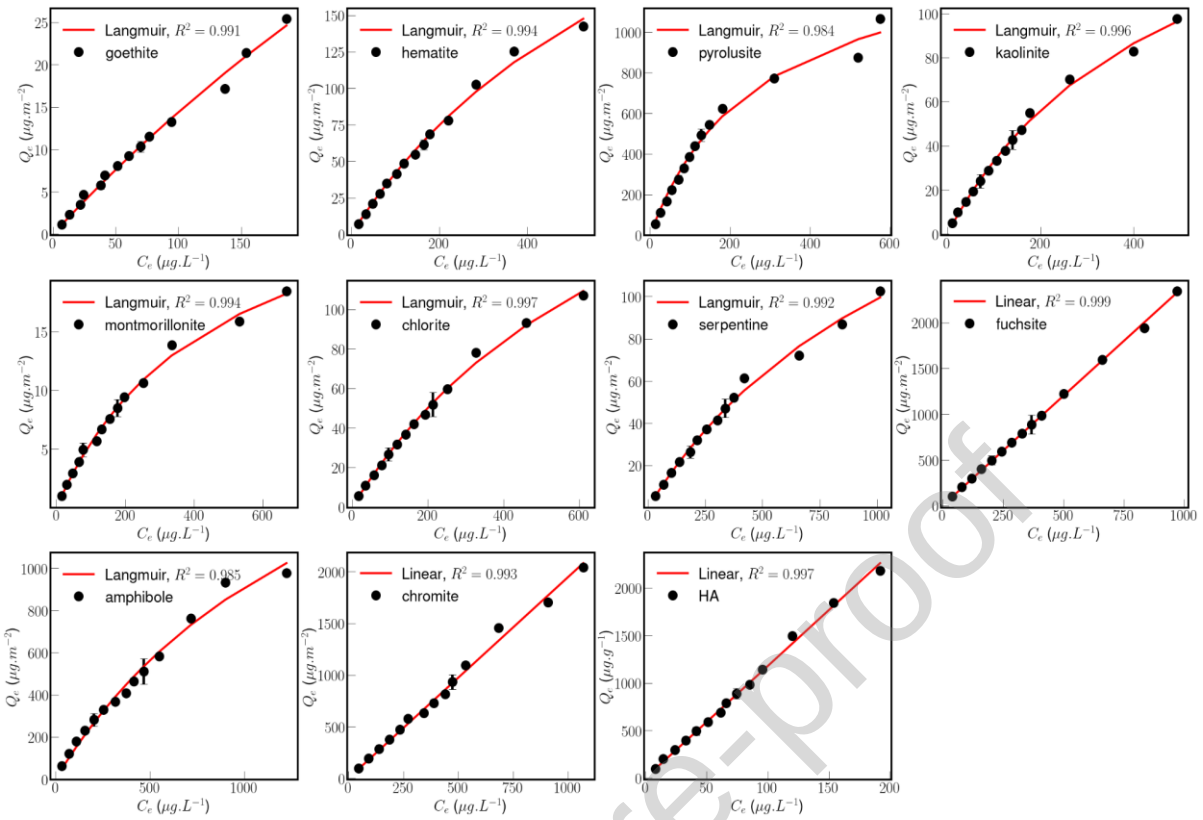

Figure 5. Isotherm data and modeling results, either with Langmuir or linear isotherm equations, for each adsorbing phase.

Langmuir sorption behaviors

Iron oxides. The maximum sorption capacities of goethite and hematite are 0.14 and 0.36 mg m^{-2}, respectively. Meanwhile, the fits provide respective values of 1.1 and 1.29 (L mg^{-1}) for the Langmuir equilibrium constant K_L. Therefore, goethite and hematite have similar affinity to Cr(III), and their Q_{max} values are also of the same order of magnitude. Metal cation binding mechanisms onto goethite and hematite are relatively well documented. Cr(III) cations can form metal binding with oxygen (hydroxyl) sites on the adsorbent surface. For goethite, its crystal presents a needle-shape with two dominant crystal planes [110] and [021] (Weidler et al., 1998). There are two type of sites based on different affinities to Cr(III): low affinity sites with high density located on the crystal plane [110] running along the needle length, and high affinity sites with low density located on the crystal plane [021] bounding the needle chains termination (Ponthieu et al., 2006; Trivedi et al., 2001). Cr(III) can form bidentate edge-sharing complexation on the [021] surface, and bidentate corner-sharing complexation on the [110] surface. It is generally considered that high affinity sites are found at the [021] plane on goethite surface (Ponthieu et al., 2006; Trivedi et al., 2001). The fact that EXAFS analysis could not

distinguish might be due to the binding of Cr to both types of site in the present conditions. On the other hand, the structure of hematite consists of hexagonal close-packing arrays of oxygen ions stacked along the [001] direction. In other words, the plane [001] has the highest proportion of sorption oxygen sites (Eggleston and Stumm, 1993), and Cr(III) can also form metal binding with such sites.

Manganese oxide. The fitting parameters for pyrolusite (Q_{max} = 1.47 mg m^{-2}, K_L = 3.0 L mg^{-1}) are higher than most of the studied phases, hence showing the strong binding of Cr to pyrolusite. Like the case of iron oxides, Cr(III) can form an inner-sphere complex on the surface of Mn oxides (pyrolusite), as suggested by Fendorf (1992) and Manceau et al. (1992), for instance. However, the complexation mechanism differs from the case of iron oxides. In particular, by analogy with Co(III), the inner-sphere complex might be expected to form at oxygen vacancy (triple-corner sharing) or at edge (double-corner sharing) sites (Simanova and Pena, 2015). Another different aspect compared to iron oxides is that Cr(III) can be partially oxidized into Cr(VI), which mainly occurs as oxyanions in aqueous solutions (Fendorf, 1992; Manceau et al., 1992). Such species can also form the corresponding inner-sphere and outer-sphere complexes on the pyrolusite surface. The existence of Cr(VI) oxyanions due to the oxidation, together with the fact that the nanostructured β-MnO_2 of pyrolusite has the most abundant oxygen vacancy concentration compared to the other nanostructures (Yang et al., 2023), might explain the large Q_{max} value of this phase in comparison to other phases.

Silicate-containing minerals. Cr(III) adsorption onto five silicate-containing minerals considered in this group are described by the nonlinear Langmuir isotherm, which equilibrium constants are K_L(montmorillonite) = 2.20, K_L(kaolinite) = 2.11, K_L(chlorite) = 1.21, K_L(serpentine) = 0.8, and K_L(amphibole) = 0.6 (L mg^{-1}). The maximum sorption capacity per SSA (mg m^{-2}) values are Q_{max}(montmorillonite) = 0.03, Q_{max}(kaolinite) = 0.19, Q_{max}(serpentine) = 0.22, Q_{max}(chlorite) = 0.26, and Q_{max}(amphibole) = 2.36 (mg m^2). In general, Cr(III) adsorbed onto phyllosilicates via two main mechanisms: electrostatic binding at cation exchange sites and surface complexation at aluminol and/or silanol group edge sites (Bolt et al., 1982; Sposito, 1984). The first type of sorption sites are permanently charged sites introduced in the siloxane surface as a result of isomorphous substitution (substitutions of Si^{4+} by Al^{3+} or Fe^{3+} in tetrahedral sites and of Al^{3+} by Mg^{2+} in octahedral sites) (Mat and Eggleton, 1999; Schoonheydt and Johnston, 2013). Cr(III) cation can form outer sphere complexes with such permanently negatively charged surface through the cation exchange reactions. This cation exchange process is favorable at low ionic strength (Gu and Evans, 2008), and is the predominant adsorption process at low pH when

H^+-dependent surface complexation is limited (Bradbury and Baeyens, 2005). Sites for the inner-sphere complexation are located on the mineral edges, and this mechanism becomes more important at high pH. Among the four phyllosilicates, serpentine has the lowest affinity, probably because it does not have a permanent negative charge due to the lack of isomorphic substitutions (Sparks and Donald, 2003). In terms of maximum adsorption capacity, the Q_{max} value of montmorillonite is one order of magnitude smaller than kaolinite, chlorite, and serpentine. According to Bradbury and Baeyens (1997), the adsorption surface complexation of montmorillonite involves two types of surface hydroxyl groups (strong sites, $\equiv S^SOH$, and weak sites, $\equiv S^WOH$) at the edges of particles. As a result, it can be concluded that the present data probes the strong sites of montmorillonite, which would also be in line with its largest K_L value among other phyllosilicates. Amphibole, on the other hand, does not belong to the phyllosilicates group, but the inosilicate group. This phase consists of 90% pargasite. The Cr(III) cations can form electrostatic attraction binding to some negative charge sites due to some possible substitutions of Si^{4+} by Al^{3+} in the tetrahedral structures. In addition, it can form the complex with the OH group located in the interiors of the rings in the double chains. The Langmuir constant is relatively low (K_L = 0.6 L mg^{-1}) compared with other phyllosilicates, but it shows the highest Q_{max} value, which might suggest surface precipitation process for the removal of Cr(III) from the solution.

Overall, K_L values display only little variation between all investigated minerals, as they range from 0.6 L mg^{-1} (amphibole) to 3.0 L mg^{-1} (pyrolusite), hence pointing to comparable adsorption processes. In fact, plotting log K_L *versus* PZC values (Figure 6) revealed a linear relationship, when excluding montmorillonite data. As PZC value depends on the proton affinity for surface sites, and relates to the surface charge of the particle, this result confirms that Cr(III) adsorption to these various phases is mostly driven by its complexation to surface -OH sites and is affected by electrosurface properties of the particles. Deviation of montmorillonite data from this trend may be attributed to the additional contribution of the cation exchange process, due to its large cation exchange capacity (Bradbury and Baeyens, 2005).

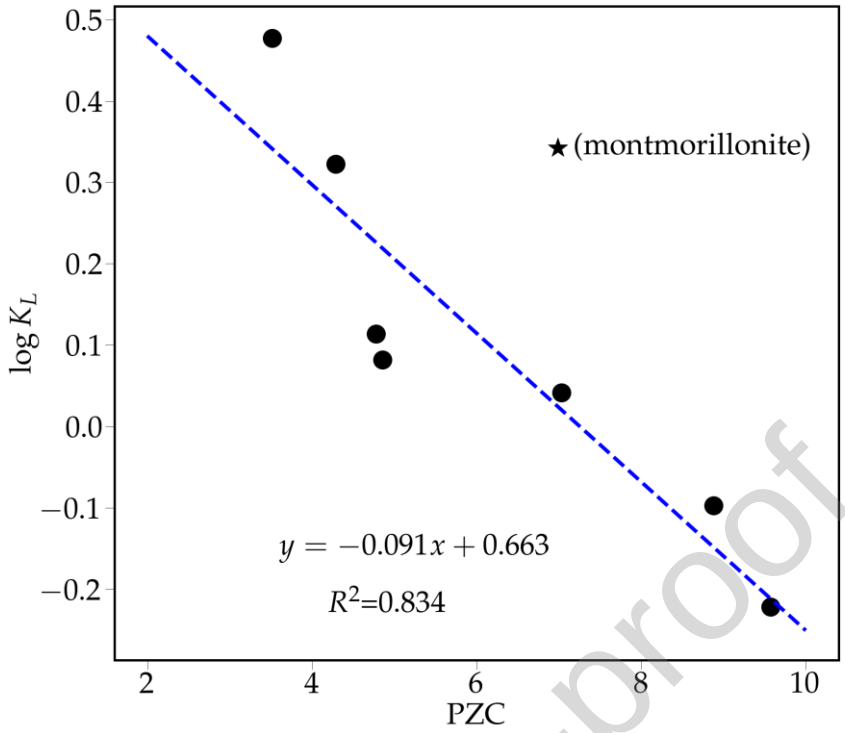

Figure 6. Plotting of log K_L *versus* PZC values

Table 3. Parameters from least-square fitting to Langmuir (Q_{max} and K_L) and linear (K_d, for fuchsite and chromite only, otherwise calculated using equation 5 for other adsorbent) isotherm models

Phases	**Linear**	**Langmuir**		
	K_d (L m^{-2})	**Q_{max}** (mg m^{-2})	**K_L** (L mg^{-1})	**R^2**
Goethite	0.15	0.14	1.10	0.991
Hematite	0.46	0.36	1.29	0.994
Pyrolusite	4.41	1.47	3.0	0.984
Kaolinite	0.4	0.19	2.11	0.996
Montmorillonite	0.07	0.03	2.20	0.994
Chlorite	0.31	0.26	1.21	0.997
Serpentine	0.18	0.22	0.80	0.992
Fuchsite	0.94	-	-	0.998
Chromite	1.95	-	-	0.993
Amphibole	1.42	2.36	0.60	0.985

Linear sorption of Cr(III) on chromite, fuchsite and HA

For the three remaining phases, the data follow linear trends without a significant nonlinear damping. The values of binding capacity K_d (in L m^{-2}) of the two mineral phases fuchsite and chromite are presented in Table 3. Meanwhile the corresponding K_d values (in L g^{-1}) of these phases together with HA are reported in Table S2. Note that adsorption capacity per SSA is not available for HA, since it is difficult to determine a reliable value for the SSA of HA. The K_d value of chromite (1.95 L m^{-2}) is greater than that of fuchsite (0.94 L m^{-2}). HA shows a rather higher binding affinity toward Cr(III) (K_d = 11.78 L g^{-1}) than those two solid phases K_d(fuchsite) = 0.57 L g^{-1}, and K_d(chromite) = 1.25 L g^{-1}). This could be explained by the fact that HA has excellent binding properties and electrostatic interactions with cations like Cr^{3+}, in addition to the formation of polymeric Cr species (Gustafsson et al., 2014).

All in all, in terms of the corresponding K_d values in L g^{-1} of adsorbents (given in the supporting data (Table S2)), the adsorption ability of the phases is of the following order: goethite> HA > pyrolusite > kaolinite > montmorillonite ~ hematite > chlorite > serpentine > chromite > amphibole > fuchsite. Generally, this ordering aligns with the above discussions on the adsorption affinity of these phases towards Cr(III).

Desorption experiments

In order to get a better knowledge of the mobility, and bioavailability of metals in natural systems, desorption experiments have been performed (Kathleen, 1999). Desorption experiments also offer an effective alternative method for investigating the presence of Cr(III) at lower concentrations, when XAS measurement cannot be performed. By quantifying the release of adsorbed species from the sample, desorption tests can provide valuable evidence of the occurrence of Cr(III) even at lower levels. Present data show that the desorption ratios are low (Figure S4), and most of the adsorbed amount of Cr(III) (> 97% whatever the solid phase considered) is retained on the surface of the phases surface under the same condition as the adsorption experiment. These desorption studies further indicated that Cr(III) was strongly bound to the mineral surfaces (Choppala et al., 2013).

4. Conclusions

The sorption of trivalent chromium by the colloidal carrying phases in ultramafic systems is a complex process involving various underlying interactions at the solid-solution interface. This research provides valuable insights into understanding the mechanisms of the sorption of trivalent chromium on Cr carrying phases in ultramafic systems. Each phase has certain predominant Cr(III) binding mechanisms, which depend greatly on its surface properties. Surface precipitation is only exhibited in the case of amphibole, and an oxidation process is observed for pyrolusite.

Chromium K-edge XANES spectra provide confirmation that Cr(III) is really adsorbed by these colloidal phases. With the exception of pyrolusite, the adsorbed Cr(III) remains unchanged and does not convert into Cr(VI) during the adsorption process. Pyrolusite is anticipated to involve the formation of Cr(VI), with roughly 10% occurring on the surface and around 1% present in solution. Desorption results also revealed that Cr(III) is strongly bound to the surface of the Cr colloids carrying phases.

The adsorption isotherms of the experiment were properly modeled using both linear and nonlinear Langmuir equations. The results emphasized that metal (hydro)oxides, phyllosilicates (with a permanent surface charge), and organic matter (HA) have a significant ability to bind Cr(III), and much higher than the primary minerals chromite, and fuchsite.

Acknowledgements.

This work was supported by the CNRT ChroNick program (CFS N°7PS2017-CNRT.IRD/CHRONICK) and EC2CO CNRS BrexIst program. Parts of this work were supported by IPGP multidisciplinary program PARI, and by Paris−IdF region SESAME Grant No. 12015908. Mrs Tuyen Nguyen's work was supported by a France Excellence Scholarship grant that covers her salary in France. Mrs Jaimy Scaria's work was supported by the COLOSSAL project funded by ANR (project number ANR-23-CE01-0001) and the French Brittany Region SAD program COLORED. The authors acknowledge the SOLEIL synchrotron for beamtime allocation at the LUCIA beamline (proposal 20230144). The authors warmly thank Ms Veni Sudarsan for obtaining and manually separating and purifying under a stereomicroscope the mineral phases of Chromite, Amphibole and Fuchsite from chromite ore samples.

References

Aharchaou, I., Py, J.-S., Cambier, S., Loizeau, J.-L., Cornelis, G., Rousselle, P., Battaglia, E., Anselmo, D., Vignati, L., 2017. Chromium hazard and risk assessment: New insights from a detailed speciation study in a standard test medium. Environ. Toxicol. Chem. 37, 983-992. https://doi.org/10.1002/etc.4044

Aiken, M.L., Abernathy, M.J., Schaefer, M.V., Lee, I., Ying, S.C., 2023. Inhibition of chromium(III) oxidation through manganese(IV) oxide passivation and iron(II) abiotic reduction. ACS Earth Space Chem. 7, 2327-2338. https://doi.org/10.1021/acsearthspacechem.3c00141

Ali, A.M., Kwaya, M.Y., Mijinyawa, A., 2021. Quartz dissolution in a single phase-high pH Berea sandstone via alkaline injection. Energy Geosci. 2, 181–188. https://doi.org/10.1016/j.engeos.2021.03.001

Alsaiari, N.S., Alzahrani, F.M., Katubi, K.M., Amari, A., Rebah, F.B., Tahoon, M.A., 2021. Polyethylenimine-modified magnetic Chitosan for the uptake of Arsenic from water. Appl. Sci. 11, 5630. https://doi.org/10.3390/app11125630

Alvarez-Silva, M., Uribe-Salas, A., Mirnezami, M., Finch, J.A., 2010. The point of zero charge of phyllosilicate minerals using the Mular-Roberts titration technique. Miner. Eng. 23, 383–389. https://doi.org/10.1016/j.mineng.2009.11.013

Ankudinov, A.L., Ravel, B., Rehr, J.J., Conradson, S.D., 1998. Real-space multiple-scattering calculation and interpretation of X-ray-absorption near-edge structure. Phys. Rev. B. 58, 7565–7576. https://doi.org/10.1103/PhysRevB.58.7565

Apte, A., Tare, V., Bose, P., 2006. Extent of oxidation of Cr(III) to Cr(VI) under various conditions pertaining to natural environment. J. Hazard. Mater. 128, 164–174. https://doi.org/10.1016/j.jhazmat.2005.07.057

Banik, N.L., Marsac, R., Lützenkirchen, J., Marquardt, C.M., Dardenne, K., Rothe, J., Bender, K., Geckeis, H., 2017. Neptunium sorption and redox speciation at the illite surface under highly saline conditions. Geochim. Cosmochim. Acta. 215, 421–431. https://doi.org/10.1016/j.gca.2017.08.008

Bartlett, R., James, B., 1979. Behavior of chromium in soils: III. Oxidation[1]. J. Environ. Qual. 8, 31–35. https://doi.org/10.2134/jeq1979.00472425000800010008x

Bayuo, J., Abukari, M.A., Pelig-Ba, K.B., 2020. Desorption of chromium (VI) and lead (II) ions and regeneration of the exhausted adsorbent. Appl. Water Sci. 10, 171. https://doi.org/10.1007/s13201-020-01250-y

Becquer, T., Quantin, C., Sicot, M., Boudot, J.P., 2003. Chromium availability in ultramafic soils from New Caledonia. Sci. Total Environ. 301, 251–261. https://doi.org/10.1016/S0048-9697(02)00298-X

Bernard, S., Chazal, P., Mazet, M., 1997. Removal of organic compounds by adsorption on pyrolusite (β-MnO_2). Water Res. 31, 1216-1222. https://doi.org/10.1016/S0043-1354(96)00149-2

Bolaños-Benítez, V., Van Hullebusch, E.D., Garnier, J., Quantin, C., Tharaud, M., Lens, P.N.L., Sivry, Y., 2018. Assessing chromium mobility in natural surface waters: Colloidal contribution to the isotopically exchangeable pool of chromium (E^{w}_{Cr} value). Appl. Geochem. 92, 19–29. https://doi.org/10.1016/j.apgeochem.2018.02.007

Bolt, M. F. Boodt, M. H. B. Hayes, M. B. McBride, E. B. A. Strooper, 1982. Interactions at the soil colloid-soil solution interface, NATO Science Series E, Applied sciences.

Bourg, I.C., Sposito, G., Bourg, A.C.M., 2007. Modeling the acid–base surface chemistry of montmorillonite. J. Colloid Interface Sci. 312, 297–310. https://doi.org/10.1016/j.jcis.2007.03.062

Bradbury, M.H., Baeyens, B., 2005. Modelling the sorption of Mn(II), Co(II), Ni(II), Zn(II), Cd(II), Eu(III), Am(III), Sn(IV), Th(IV), Np(V) and U(VI) on montmorillonite: Linear free energy relationships and estimates of surface binding constants for some selected heavy metals and actinides. Geochim. Cosmochim. Acta. 69, 875–892. https://doi.org/10.1016/j.gca.2004.07.020

Bradbury, M.H., Baeyens, B., 1997. A mechanistic description of Ni and Zn sorption on Na-montmorillonite Part II: modelling. J. Contam. Hydrol. 27, 223–248. https://doi.org/10.1016/S0169-7722(97)000

Charlet, L., Manceau, A.A., 1992. X-ray absorption spectroscopic study of the sorption of Cr(III) at the oxide-water interface. J. Colloid Interface Sci. 148, 443–458. https://doi.org/10.1016/0021-9797(92)90182-L

Chen, S., Wu, Y., Cui, P., Chu, W., Chen, X., Wu, Z., 2013. Cation distribution in $ZnCr_2O_4$ nanocrystals investigated by X-ray absorption fine structure spectroscopy. J. Phys. Chem. C. 117, 25019-25025. https://doi.org/10.1021/jp404984y

Choppala, G., Bolan, N., Park, J.H., 2013. Chromium contamination and its risk management in complex environmental settings. Adv. Agron. 120, 129-172. https://doi.org/10.1016/B978-0-12-407686-0.00002-6

Chrysochoou, M., Theologou, E., Bompoti, N., Dermatas, D., Panagiotakis, I., 2016. Occurrence, origin and transformation processes of geogenic chromium in soils and sediments. Curr. Pollut. Rep. 2, 224-235. https://doi.org/10.1007/s40726-016-0044-2

Covelo, E.F., Vega, F.A., Andrade, M.L., 2007. Competitive sorption and desorption of heavy metals by individual soil components. J. Hazard. Mater. 140, 308-315. https://doi.org/10.1016/j.jhazmat.2006.09.018

Dayan, A., Paine, A., 2001. Mechanisms of chromium toxicity, carcinogenicity and allergenicity: Review of the literature from 1985 to 2000. Hum Exp Toxicol. 20, 439-451. https://doi.org/doi: 10.1191/096032701682693062

Do, D.D., 1998. Adsorption analysis: equilibria and kinetics, Chemical Engineering. Imperial College Press.

Dzieniszewska, A., Kyziol-Komosinska, J., Pająk, M., 2020. Adsorption and bonding strength of chromium species by ferrihydrite from acidic aqueous solutions. PeerJ 8, e9324. https://doi.org/10.7717/peerj.9324

Eggleston, Stumm, 1993. Scanning tunneling microscopy of Cr(III) chemisorbed on α-Fe_2O_3 (001) surfaces from aqueous solution: Direct observation of surface mobility and clustering. Geochim. Cosmochim. Acta. 57, 4843-4850. https://doi.org/10.1016/0016-7037(93)90203-9

Elmaalouf, M., Odziomek, M., Duran, S., Gayrard, M., Bahri, M., Tard, C., Zitolo, A., Lassalle-Kaiser, B., Piquemal, J.-Y., Ersen, O., Boissière, C., Sanchez, C., Giraud, M., Faustini, M., Peron, J., 2021. The origin of the high electrochemical activity of pseudo-amorphous iridium oxides. Nat. Commun. 12, 3935. https://doi.org/10.1038/s41467-021-24181-x

Fendorf, S.E., 1995. Surface reactions of chromium in soils and waters. Geoderma. 67, 55-71. https://doi.org/10.1016/0016-7061(94)00062-F

Fendorf, S.E., 1992. Inhibitory mechanisms of Cr(III) oxidation by δ-MnO_2. J. Colloid Interface Sci.

153, 37–54. https://doi.org/10.1016/0021-9797(92)90296-X

Feng, B., Feng, Q., Lu, Y., 2012. A novel method to limit the detrimental effect of serpentine on the flotation of pentlandite. Int. J. Miner. Process. 114-117, 11-13. https://doi.org/10.1016/j.minpro.2012.08.001

Fitts, J.P., Brown, G.E., Parks, G.A., 2000. Structural evolution of Cr(III) polymeric species at the γ-Al_2O_3 /Water Interface. Environ. Sci. Technol. 34, 5122–5128. https://doi.org/10.1021/es9914285

Flank, A.M., Cauchon, G., Lagarde, P., Bac, S., Janousch, M., Wetter, R., Dubuisson, J.M., Idir, M., Langlois, F., Moreno, T., Vantelon, D., 2006. LUCIA, a microfocus soft XAS beamline. Nucl. Instrum. Methods Phys. Res. Sect. B Beam Interact. Mater. At. 246, 269–274. https://doi.org/10.1016/j.nimb.2005.12.007

García-Guaderrama, M., Montero-Cabrera, M.E., Morán, E., Alario-Franco, M.A., Fuentes-Cobas, L.E., Macías-Ríos, E., Esparza-Ponce, H.E., Fuentes-Montero, M.E., 2015. Long - and short-range structure of ferrimagnetic iron-chromium maghemites. Inorg. Chem. 54, 11200–11208. https://doi.org/10.1021/acs.inorgchem.5b01624

Garnier, J., Quantin, C., Raous, S., Guimarães, E., Becquer, T., 2021. Field availability and mobility of metals in Ferralsols developed on ultramafic rock of Niquelândia, Brazil. Braz. J. Geol. 51. https://doi.org/10.1590/2317-4889202120200092

Gheju, M., Balcu, I., Mosoarca, G., 2016. Removal of Cr(VI) from aqueous solutions by adsorption on MnO_2. J. Hazard. Mater. 310, 270–277. https://doi.org/10.1016/j.jhazmat.2016.02.042

Glasauer, S., Friedl, J., Schwertmann, U., 1999. Properties of goethites prepared under acidic and basic conditions in the presence of silicate. J. Colloid Interface Sci. 216, 106–115. https://doi.org/10.1006/jcis.1999.6285

Gu, X., Evans, L.J., 2008. Surface complexation modelling of Cd(II), Cu(II), Ni(II), Pb(II) and Zn(II) adsorption onto kaolinite. Geochim. Cosmochim. Acta. 72, 267–276. https://doi.org/10.1016/j.gca.2007.09.032

Gunawardana, C., Goonetilleke, A., Egodawatta, P., 2013. Adsorption of heavy metals by road deposited solids. Water Sci. Technol. 67, 2622–2629. https://doi.org/10.2166/wst.2013.171

Guo, H., Liu, C., Yan, S., Yin, J., Shan, J., 2024. Source, distribution, and geochemical processes of geogenic high chromium groundwater around the world: A critical review. J. Hydrol. 638, 131480. https://doi.org/10.1016/j.jhydrol.2024.131480

Guo, Li, Wu, W., 2009. Sorption of U(VI) on goethite: Effects of pH, ionic strength, phosphate, carbonate and fulvic acid. Appl. Radiat. Isot. 67, 996-1000. https://doi.org/10.1016/j.apradiso.2009.02.001

Gustafsson, J.P., Persson, I., Kleja, D.B., van Schaik, J.W.J., 2007. Binding of iron(III) to organic soils: EXAFS spectroscopy and chemical equilibrium modeling. Environ. Sci. Technol. 41, 1232–1237. https://doi.org/10.1021/es0615730

Gustafsson, J.P., Persson, I., Oromieh, A.G., Van Schaik, J.W.J., Sjöstedt, C., Kleja, D.B., 2014. Chromium(III) complexation to natural organic matter: Mechanisms and modeling. Environ. Sci. Technol. 48, 1753–1761. https://doi.org/10.1021/es404557e

Hao, W., Chen, N., Sun, W., Mänd, K., Kirsimäe, K., Teitler, Y., Somelar, P., Robbins, L.J., Babechuk, M.G., Planavsky, N.J., Alessi, D.S., Konhauser, K.O., 2022. Binding and transport of Cr(III) by clay minerals during the Great Oxidation Event. Earth Planet. Sci. Lett. 584, 117503. https://doi.org/10.1016/j.epsl.2022.117503

Hao, Y., Ma, H., Wang, Q., Zhu, C., He, A., 2022. Complexation behaviour and removal of organic-Cr(III) complexes from the environment: A review. Ecotoxicol. Environ. Saf. 240, 113676. https://doi.org/10.1016/j.ecoenv.2022.113676

Hiemstra, T., De Wit, J.C.M., Van Riemsdijk, W.H., 1989. Multisite proton adsorption modeling at the solid/solution interface of (hydr)oxides: A new approach. J. Colloid Interface Sci. 133, 91–104. https://doi.org/10.1016/0021-9797(89)90284-1

Holmgren, G.G.S., 1967. A rapid citrate-dithionite extractable iron procedure. Soil Sci. Soc. Am. J. 31, 210–211. https://doi.org/10.2136/sssaj1967.03615995003100020020x

Islam, M.A., Angove, M.J., Morton, D.W., Pramanik, B.K., Awual, M.R., 2020. A mechanistic approach of chromium (VI) adsorption onto manganese oxides and boehmite. J. Environ. Chem. Eng. 8, 103515. https://doi.org/10.1016/j.jece.2019.103515

Johnston, C.P., Chrysochoou, M., 2012. Investigation of chromate coordination on ferrihydrite by in situ ATR-FTIR spectroscopy and theoretical frequency calculations. Environ. Sci. Technol. 46, 5851–5858. https://doi.org/10.1021/es300660r

Kar, S., Equeenuddin, S.M., 2019. Adsorption of hexavalent chromium using natural goethite: Isotherm, thermodynamic and kinetic study. J. Geol. Soc. India. 93, 285–292. https://doi.org/10.1007/s12594-019-1175-z

Kathleen, S.S., 1999. Metal sorption on mineral surfaces: An overview with examples relating to mineral deposits, in: Economic Geology. pp. 161–182.

Kinniburgh, D.G., Cooper, D.M., 2011. PhreePlot Creating graphical output with PHREEQC.

Ko, I., Kim, J.Y., Kim, K.W., 2005. Adsorption properties of soil humic and fulvic acids by hematite. Chem. Speciat. Bioavailab. 17, 41–48. https://doi.org/10.3184/095422905782774928

Koppelman, M.H., Emerson, A.B., Dillard, J.G., 1980. Adsorbed Cr(III) on chlorite, illite, and kaolinite: An X-Ray photoelectron spectroscopic study. Clays Clay Miner. 28, 119–124.

Kosmulski, M., Durand-Vidal, S., Maczka, E., Rosenholm, J.B., 2004. Morphology of synthetic goethite particles. J. Colloid Interface Sci. 271, 261–269. https://doi.org/10.1016/j.jcis.2003.10.032

Landrot, G., 2018. FASTOSH: a software to process XAFS data for geochemical & environmental applications. https://goldschmidtabstracts.info/2018/1402.pdf

Liang, J., Huang, X., Yan, J., Li, Y., Zhao, Z., Liu, Y., Ye, J., Wei, Y., 2021. A review of the formation of Cr(VI) via Cr(III) oxidation in soils and groundwater. Sci. Total Environ. 774, 145762. https://doi.org/10.1016/j.scitotenv.2021.145762

Manceau, A., Charlet, L., Boisset, M.C., Didier, B., Spadini, L., 1992. Sorption and speciation of heavy metals on hydrous Fe and Mn oxides. From microscopic to macroscopic. Appl. Clay Sci. 7, 201–223. https://doi.org/10.1016/0169-1317(92)90040-T

Marsac, R., Catrouillet, C., Pédrot, M., Benedetti, M.F., Dia, A., Van Hullebusch, E.D., Davranche, M., Sivry, Y., Pierson-Wickmann, A.-C., Tharaud, M., Heberling, F., 2024. Equilibrium surface complexation modeling with metastable natural colloids: The key to predict the oxidation state distribution of trace elements? Curr. Opin. Colloid Interface Sci. 72, 101820. https://doi.org/10.1016/j.cocis.2024.101820

Mat, C., Eggleton, R.A., 1999. Cation exchange capacity of kaolinite. Clays Clay Miner. 47, 174–180. https://doi.org/DOI:10.1346/CCMN.1999.0470207

Mikutta, C., Kretzschmar, R., 2011. Spectroscopic evidence for ternary complex formation between

arsenate and ferric iron complexes of humic substances. Environ. Sci. Technol. 45, 9550–9557. https://doi.org/10.1021/es202300w

Miranda, L.S., Ayoko, G.A., Egodawatta, P., Goonetilleke, A., 2022. Adsorption-desorption behavior of heavy metals in aquatic environments: Influence of sediment, water and metal ionic properties. J. Hazard. Mater. 421, 126743. https://doi.org/10.1016/j.jhazmat.2021.126743

Monga, A., Fulke, A.B., Dasgupta, D., 2022. Recent developments in essentiality of trivalent chromium and toxicity of hexavalent chromium: Implications on human health and remediation strategies. J. Hazard. Mater. Adv. 7, 100113. https://doi.org/10.1016/j.hazadv.2022.100113

Namgung, S., Kwon, M.J., Qafoku, N.P., Lee, G., 2014. $Cr(OH)_3(s)$ oxidation induced by surface catalyzed Mn(II) oxidation. Environ. Sci. Technol. 48, 10760-10768. https://doi.org/10.1021/es503018u

Oze, C., Fendorf, S., Bird, D.K., Coleman, R.G., 2004. Chromium geochemistry in serpentinized ultramafic rocks and serpentine soils from the Franciscan complex of California. Am. J. Sci. 304, 67–101. https://doi.org/10.2475/ajs.304.1.67

Papassiopi, N., Pinakidou, F., Katsikini, M., Antipas, G.S.E., Christou, C., Xenidis, A., Paloura, E.C., 2014. A XAFS study of plain and composite iron(III) and chromium(III) hydroxides. Chemosphere. 111, 169–176. https://doi.org/10.1016/j.chemosphere.2014.03.059

Parkhurst, D.L., Appelo, C.A.J., 1999. User's guide to PHREEQC (Version 2): A computer program for speciation, batch-reaction, one-dimensional transport, and inverse geochemical calculations (USGS Numbered Series), Water-Resources Investigations Report. https://doi.org/10.3133/wri994259

Ponthieu, M., Juillot, F., Hiemstra, T., van Riemsdijk, W.H., Benedetti, M.F., 2006. Metal ion binding to iron oxides. Geochim. Cosmochim. Acta. 70, 2679–2698. https://doi.org/10.1016/j.gca.2006.02.021

Quantin, C., Garnier, J., Bolanos Benitez, V., Gelabert, A., Adjei Mensah, E., Sivry, Y., Juillot, F., Morin, G., Krishnan, S., Subramanian, S., 2021. Environmental dynamics of chromium in ultramafic systems: A combined approach, in: Goldschmidt2021 Abstracts. Presented at the Goldschmidt2021, European Association of Geochemistry, Virtual. https://doi.org/10.7185/gold2021.3738

Rao, F., Song, S., Lopez-Valdivieso, A., 2012. Specific adsorption of chromium species on kaolinite surface. Miner. Process. Extr. Metall. Rev. 33, 180-189. https://doi.org/10.1080/08827508.2011.562949

Raous, S., Echevarria, G., Sterckeman, T., Hanna, K., Thomas, F., Martins, E.S., Becquer, T., 2013. Potentially toxic metals in ultramafic mining materials: Identification of the main bearing and reactive phases. Geoderma. 192, 111–119. https://doi.org/10.1016/j.geoderma.2012.08.017

Ratié, G., Zhang, K., Iqbal, M., Vantelon, D., Mahé, F., Rivard, C., Komárek, M., Bouhnik-Le Coz, M., Dia, A., Hanna, K., Davranche, M., Marsac, R., 2023. Driving forces of Ce(III) oxidation to Ce(IV) onto goethite. Chem. Geol. 633, 121547. https://doi.org/10.1016/j.chemgeo.2023.121547

Ravel, B., Newville, M., 2005. *ATHENA*, *ARTEMIS*, *HEPHAESTUS*: data analysis for X-ray absorption spectroscopy using *IFEFFIT*. J. Synchrotron Radiat. 12, 537-541. https://doi.org/10.1107/S0909049505012719

Schaefer, M.V., Handler, R.M., Scherer, M.M., 2017. Fe(II) reduction of pyrolusite (β-MnO_2) and secondary mineral evolution. Geochem. Trans. 18. https://doi.org/10.1186/s12932-017-0045-0

Schoonheydt, R.A., Johnston, C.T., 2013. Surface and interface chemistry of clay minerals, in: Developments in Clay Science. Elsevier B.V., pp. 139–172. https://doi.org/10.1016/B978-0-08-098258-8.00005-5

Seif, S., Marofi, S., Mahdavi, S., 2019. Removal of Cr^{3+} ion from aqueous solutions using MgO and montmorillonite nanoparticles. Environ. Earth Sci. 78, 377. https://doi.org/10.1007/s12665-019-8380-3

Simanova, A.A., Pena, J., 2015. Time-resolved investigation of cobalt oxidation by Mn(III)-rich δ-MnO_2 using quick X-ray absorption spectroscopy. Environ. Sci. Technol. 49, 10867–10876. https://doi.org/10.1021/acs.est.5b01088

Singh, B., Mackinnon, I.D.R., 1996. Experimental transformation of kaolinite to halloysite. Clays Clay Miner. 44, 825–834. https://doi.org/10.1346/CCMN.1996.0440614

Smičiklas, I.D., Milonjicámilonjicá, S.K., Pfendt, P., Raičevicá, S.R., 2000. The point of zero charge and sorption of cadmium(II) and strontium(II) ions on synthetic hydroxyapatite. Sep. Purif. Technol. 19, 185–194. https://doi.org/10.1016/S1383-5866(99)00066-0

Souza, R.F., Brandão, P.R.G., Paulo, J.B.A., 2012. Effect of chemical composition on the ζ-potential of chromite. Miner. Eng. 36–38, 65–74. https://doi.org/10.1016/j.mineng.2012.02.012

Sparks, Donald L, 2003. Environmental Soil Chemistry. Academic Press.

Sposito, G., 1984. The Surface Chemistry of Soils. Clays and Clay Minerals.

Sun, Z., Chunshui, Z., Jiangbo, H., Wenqi, G., Hesheng, C., Shanbin, M.U., 2006. A study of chromium adsorption on natural goethite biomineralized with iron bacteria. Acta Geol. Sin. 80, 597–603. https://doi.org/10.1111/j.1755-6724.2006.tb00280.x

Thommes, M., Kaneko, K., Neimark, A.V., Olivier, J.P., Rodriguez-Reinoso, F., Rouquerol, J., Sing, K.S.W., 2015. Physisorption of gases, with special reference to the evaluation of surface area and pore size distribution (IUPAC Technical Report). Pure Appl. Chem. 87, 1051–1069. https://doi.org/doi:10.1515/pac-2014-1117

Trivedi, P., Axe, L., Dyer, J., 2001. Adsorption of metal ions onto goethite: single-adsorbate and competitive systems. Colloids Surf. Physicochem. Eng. Asp. 191, 107–121. https://doi.org/10.1016/S0927-7757(01)00768-3

Ugbe, F.A., Abdus-Salam, N., 2018. Characterization of synthesized goethite and natural goethite sourced from Itakpe in North Central, Nigeria. ChemSearch J. 9, 24 - 32.

Vantelon, D., Trcera, N., Roy, D., Moreno, T., Mailly, D., Guilet, S., Metchalkov, E., Delmotte, F., Lassalle, B., Lagarde, P., Flank, A.M., 2016. The LUCIA beamline at SOLEIL. J. Synchrotron Radiat. 23, 635–640. https://doi.org/10.1107/S1600577516000746

Veselská, V., Fajgar, R., Číhalová, S., Bolanz, R.M., Göttlicher, J., Steininger, R., Siddique, J.A., Komárek, M., 2016. Chromate adsorption on selected soil minerals: Surface complexation modeling coupled with spectroscopic investigation. J. Hazard. Mater. 318, 433–442. https://doi.org/10.1016/j.jhazmat.2016.07.002

Vieira, A.P., Berndt, G., De Souza Junior, I.G., Di Mauro, E., Paesano, A., De Santana, H., Da Costa, A.C.S., Zaia, C.T.B.V., Zaia, D.A.M., 2011. Adsorption of cysteine on hematite, magnetite and ferrihydrite: FT-IR, Mössbauer, EPR spectroscopy and X-ray diffractometry studies. Amino Acids. 40, 205–214. https://doi.org/10.1007/s00726-010-0635-y

Vlachos, A., Psycharis, V., Raptopoulou, C.P., Lalioti, N., Sanakis, Y., Diamantopoulos, G., Fardis, M., Karayanni, M., Papavassiliou, G., Terzis, A., 2004. A nearly symmetric trinuclear

chromium(III) oxo carboxylate assembly: preparation, molecular and crystal structure, and magnetic properties of $[Cr_3O(O_2CPh)_6(MeOH)_3](NO_3)\cdot 2MeOH$. Inorganica Chim. Acta. 357, 3162–3172. https://doi.org/10.1016/j.ica.2004.04.005

Weerasooriya, R., Tobschall, H.J., 2000. Mechanistic modeling of chromate adsorption onto goethite. Colloids Surf. Physicochem. Eng. Asp. 162, 167–175. https://doi.org/10.1016/S0927-7757(99)00229-0

Weidler, P.G., Hug, S.J., Wetche, T.P., Hiemstra, T., 1998. Determination of growth rates of (100) and (110) faces of synthetic goethite by scanning force microscopy. Geochim. Cosmochim. Acta. 62, 3407–3412. https://doi.org/10.1016/S0016-7037(98)00251-8

Yang, P., Wang, J., Wang, H., Wang, S., Yang, C., He, Y., 2023. Physicochemical properties of different crystal forms of manganese dioxide prepared by a liquid phase method and their quantitative evaluation in capacitor and battery materials. Nanoscale Adv. 5, 3396–3413. https://doi.org/10.1039/d3na00144j

Zachara, J.M., Cowan, C.E., Schmidt, R.L., Ainsworth, C.C., 1988. Chromate adsorption by kaolinite. Clays Clay Miner. 36, 317–326. https://doi.org/10.1346/CCMN.1988.0360405

Zelano, I.O., Sivry, Y., Quantin, C., Gélabert, A., Maury, A., Phalyvong, K., Benedetti, M.F., 2016. An isotopic exchange kinetic model to assess the speciation of metal available pool in soil: The case of Nickel. Environ. Sci. Technol. 50, 12848–12856. https://doi.org/10.1021/acs.est.6b02578

Zhang, J., Yin, H., Barnie, S., Wei, M., Chen, H., 2019. Mechanism and modeling of hexavalent chromium interaction with a typical black soil: the importance of the relationship between adsorption and reduction. RSC Adv. 9, 5582–5591. https://doi.org/10.1039/c8ra08154a

Zhu, H., Xiao, X., Guo, Z., Han, X., Liang, Y., Zhang, Y., Zhou, C., 2018. Adsorption of vanadium (V) on natural kaolinite and montmorillonite: Characteristics and mechanism. Appl. Clay Sci. 161, 310–316. https://doi.org/10.1016/j.clay.2018.04.035

Declaration of interests

☒ The authors declare that they have no known competing financial interests or personal relationships that could have appeared to influence the work reported in this paper.

Highlights:

- Cr(III) sorption to ten mineral phases and humic acid was investigated.

- Binding mechanisms depend on the surface properties of each phase.

- Only pyrolusite partially oxidized Cr(III) to Cr(VI); Cr(III) persisted with other phases.

- Cr K-edge XAS spectroscopy indicates Cr(III) surface complexation process

- Sorption isotherms could be predicted with Langmuir or linear isotherm equations.